A bulk microfabricated multi-axis capacitive cellular force sensor using transverse comb drives

2002 J. Micromech. Microeng. 12 832

(http://iopscience.iop.org/0960-1317/12/6/314)

INSTITUTE OF PHYSICS PUBLISHING JOURNAL OF MICROMECHANICS AND MICROENGINEERING
J. Micromech. Microeng. **12** (2002) 832–840 PII: S0960-1317(02)35710-3

A bulk microfabricated multi-axis capacitive cellular force sensor using transverse comb drives

Yu Sun[1], Bradley J Nelson[1], David P Potasek[1] and Eniko Enikov[2]

[1] Department of Mechanical Engineering, University of Minnesota, 111 Church Street SE, Minneapolis, MN 55455, USA
[2] Aerospace and Mechanical Engineering, University of Arizona, 1130 N Mountain, Tucson, AZ 85721, USA

E-mail: yus@me.umn.edu

Received 9 April 2002, in final form 7 August 2002
Published 3 October 2002
Online at stacks.iop.org/JMM/12/832

Abstract
This paper presents design, fabrication and calibration results for a novel 2-DOF capacitive force sensor capable of resolving forces up to 490 μN with a resolution of 0.01 μN in x, and up to 900 μN with a resolution of 0.24 μN in y. A simple fabrication process using deep reactive ion etching (DRIE) on silicon-on-insulator (SOI) wafers forms the 3D high aspect ratio structure. A transverse mode comb drive movement is used to greatly improve device sensitivity. Among other advantages of the developed process is a dice-free release of wafer structures, allowing fragile structures to be individually packaged. Notching or footing effects and bowing effects are well-known problems in DRIE on SOI wafers. Techniques to overcome notching and bowing effects using a PlasmaTherm SLR-770 etcher are presented that do not require hardware modifications. The application of the force sensor is for providing real-time force feedback during individual cell manipulation tasks.

1. Introduction

When autonomously manipulating objects, force feedback almost always improves the speed and robustness with which the manipulation task is performed. When manipulating objects ranging in size from microns to nanometers, force information is difficult to measure and is typically obtained along a single axis using laser-based optical force measurement techniques or piezoresistive devices. Recent advances in microbiology, such as cloning, require increasingly complex micromanipulation strategies for manipulating individual biological cells. Although multi-axis force sensing capabilities would be useful for handling cells by providing information on probing forces as well as tangential forces generated by improperly aligned cell probes, no sensors capable of multi-axis force sensing at the force scales required are available. This paper describes the design and fabrication of a 2-DOF capacitive cellular force sensor for microrobotic cell manipulation.

For cellular force measurement, cantilevers are the most frequently implemented MEMS devices. The main sensing mechanisms used with cantilevers are optical, piezoresistive and piezoelectric methods. Cantilever-based optical force sensors and piezoresistive force sensors have been reported for cellular force measurement [1–5]. Cantilever-based optical force measurement often uses atomic force microscopy (AFM) techniques. There are three limitations restricting AFM use in cellular force measurement. First, a major requirement in AFM measurement is that a complex transmit–receive setup is required. This setup places a high demand on optical alignment and adjustment. The surface of the cantilever must also be sufficiently reflective to achieve high accuracy. Second, an important system limitation is that the photodiode can only detect a small range of deflection. This constrains the force measurement range. Third, when an AFM is used in aqueous mediums where biological cells survive, the reflection and refraction of the transmitted light make the accuracy of cellular force measurements problematic.

Even though widely used, almost all existing cantilever-based cellular force sensors are only capable of measuring forces perpendicular to the sensor plane. To provide multi-axis force information and avoid the limitations of atomic force microscopy, a multi-axis capacitive cellular force sensor has been designed and fabricated. A complete set of simulation and characterization results on four device geometries is reported in this paper. A capacitive cellular force sensor design was previously reported in [6]. Our design differs from that of [6] in device geometry, sensitivity resolution, fabrication sequence and readout circuit design. To convert force into a relatively large capacitance change, the capacitive cellular force sensor employs an interdigitated transverse comb drive structure.

Polysilicon surface micromachining has been widely applied to form interdigitated comb drive structures. However, the thinness of the deposited polysilicon film limits certain aspects of device performance, such as capacitive sensing sensitivity, because of the small overlapping area between each pair of parallel plates [7–11]. In addition, the use of polysilicon creates material and fabrication issues that do not appear in bulk micromachining processes, such as residual stress, stress gradient through the film, variation of Young's modulus, topography variations with multiple-layer structures, and stiction [10]. To overcome these limitations, many processes have been developed and successfully adopted to form high aspect ratio comb drive structures including the SCREAM process [12, 13], the dissolved wafer process [14], the etch-diffusion process [15], the surface/bulk micromachining process [16, 17] and molding processes such as LIGA [18] and HEXSIL [19].

This paper reports on a simple process using deep reactive ion etching (DRIE) on silicon-on-insulator (SOI) to form high aspect ratio suspending interdigitated comb drive structures. The comb fingers are 50 μm in depth, greatly increasing sensitivity because of the large overlapping area. An aspect ratio of more than 100 can be achieved using the developed process, which is a dice-free release of wafer structures, allowing fragile structures to be individually packaged. Though bulk micromachining does not have the inherent surface micromachining problems such as stiction, DRIE on SOI wafers demonstrates two well-known phenomena, i.e., notching or footing effects and bowing effects [20–24]. In this paper, techniques are proposed to overcome these effects.

Besides the depth difference of comb parallel plates, another major difference between this capacitive cellular force sensor and the other reported devices using the interdigitated comb drive structure is the movement mode of the capacitive plates. Transverse movement of the movable plates is adopted instead of lateral mode of movement [7–10, 14]. A lateral movement of movable plates changes the overlapping area of a parallel plate capacitor. The main advantage of comb drive's lateral movement is the achievement of linearity between area change and capacitance change. The multi-axis force sensor design presented in this paper is based on transverse movement of the movable plates rather than lateral movement. This gap change between plates provides higher sensitivity, and the linear relationship between the gap change and capacitance change can be maintained for small displacements of the movable plates.

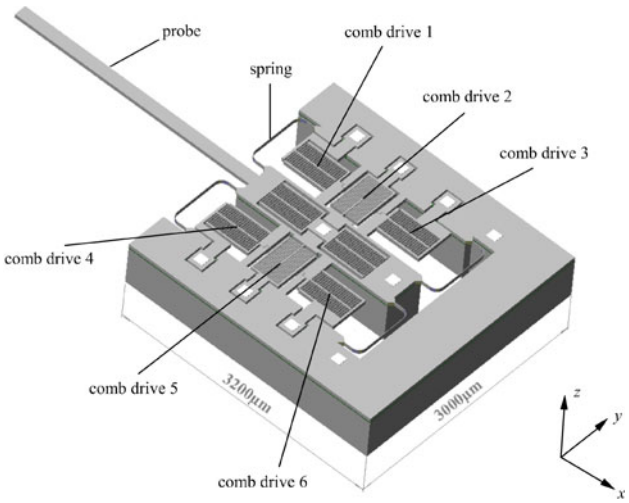

Figure 1. Solid model of the multi-axis force sensor.

2. Cellular force sensor design

The multi-axis capacitive force sensor has been designed and developed to provide real-time force feedback during cell manipulation. According to the elastic modulus estimation on lipid bilayer membrane [25], an external load of 0.215–11 μN causes a 5 μm deformation. In order to accommodate a larger range of forces for characterizing cell membrane properties, four configurations of the capacitive force sensor have been designed and fabricated to measure forces up to 490 μN with a resolution of 0.01 μN in x, and up to 900 μN with a resolution of 0.24 μN in y.

Figure 1 shows the solid model of the force sensor design. The constrained outer frame and the inner movable plate are connected by four curved springs. A load applied on the probe causes the movable plate to move, changing the gap between each pair of the interdigitated comb capacitors. Consequently, the total capacitance change resolves the applied force. By varying the dimensions of the springs to change device stiffness, a large range of forces can be resolved. To make the force sensor capable of resolving forces in both x and y directions, the interdigitated capacitors are configured to be orthogonal to each other as shown in figure 2. Note that the two comb drive capacitors located in the movable plate providing reference capacitance for the readout circuit are not for sensing use.

2.1. Structural analysis

A structural analysis of the device has been conducted using finite element simulations. Figure 3 illustrates the relationship between applied forces and corresponding displacements.

In the design process, several spring designs were considered besides the curved spring design shown in figure 1. Though the devices with straight springs, which are straight beams having the same length, width and depth as the curved springs, pose less difficulty for mask design and microfabrication, comparisons between the curved spring design and the straight spring design show that the curved

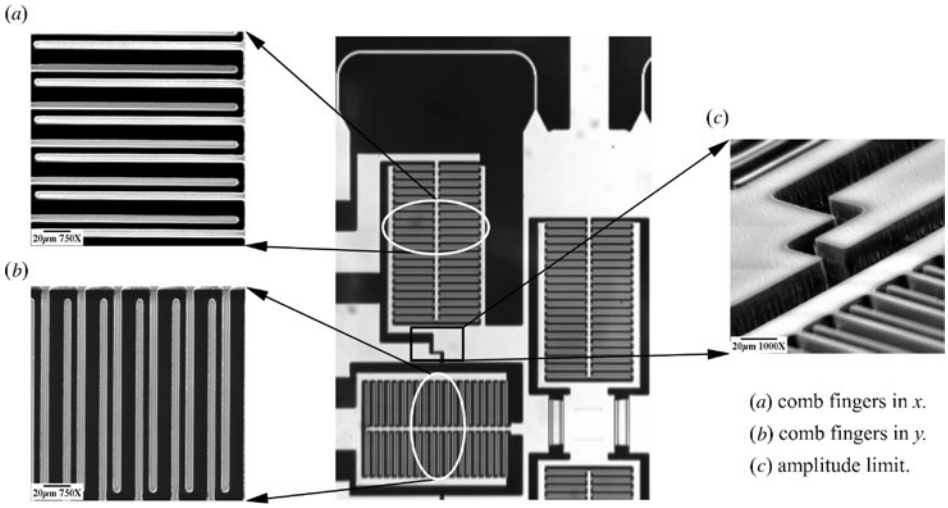

Figure 2. Orthogonal configuration of offset comb drives.

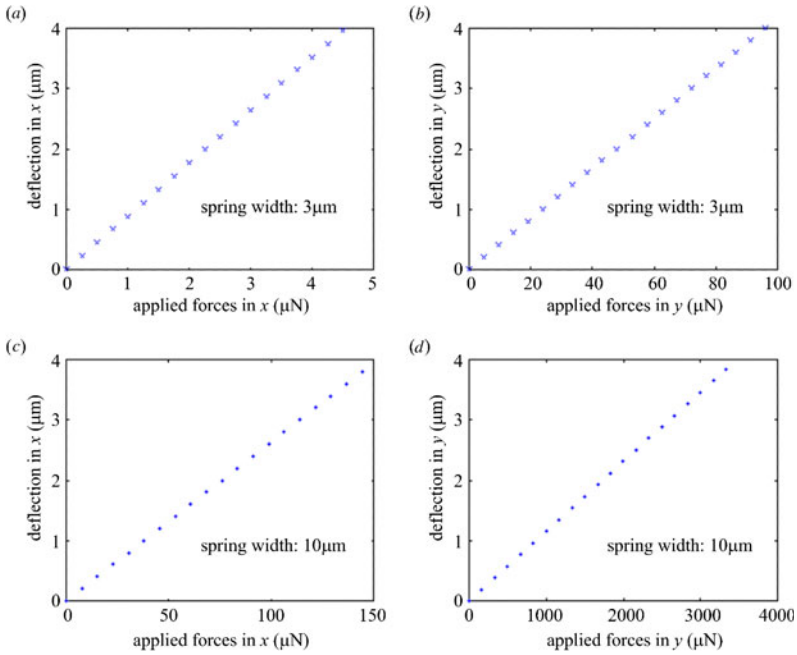

Figure 3. Applied forces and corresponding deflections: (*a*) and (*b*) spring width = 3 μm; (*c*) and (*d*) spring width = 10 μm.

spring design has a sensitivity as high as three times that of the straight spring design as shown in figure 4.

The force-deflection model of the spring in both x and y is

$$\delta = \lambda \frac{F}{Et^3 h} \tag{1}$$

where δ is the deflection, F is the applied force, $E = 125$ GPa is the Young's modulus of silicon, $t = 3, 5, 7, 10\,\mu$m is the width of the springs giving four device configurations, $h = 50\,\mu$m is the height of the springs and λ is a constant. Table 1 lists the values of λ in x and y for the curved and straight spring designs determined by finite element analysis (FEA).

Due to its higher sensitivity in both x and y, the curved spring design was adopted. By varying the spring dimensions, a large range of displacements can be achieved for a given applied force.

Table 1. Values of λ in equation (1).

Design	λ in x (m^3)	λ in y (m^3)
Curved	2.359×10^{-10}	1.101×10^{-11}
Straight	6.573×10^{-11}	3.553×10^{-12}

2.2. Electrostatic analysis

In order to enable the force sensor to measure forces in both x and y directions, capacitance selectivity must be achieved. Offset comb capacitors are used.

If the fringing fields are neglected, the total capacitance of the configuration shown in figure 5, where the middle plate moves in the positive x direction under a load, is given by

$$C_{\text{total}} = C_1 + C_2 = K\varepsilon \frac{(h - |\Delta y|)(w - |\Delta z|)(d_1 + d_2)}{[-\Delta x^2 - \Delta x(d_1 - d_2) + d_1 d_2]} \tag{2}$$

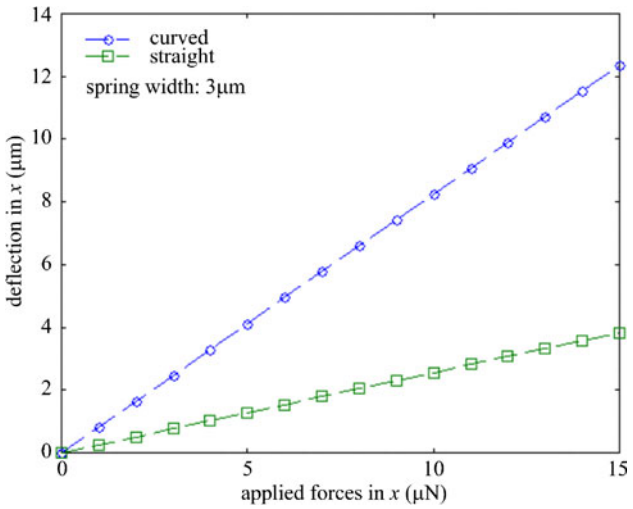

Figure 4. Curved and straight spring designs in x.

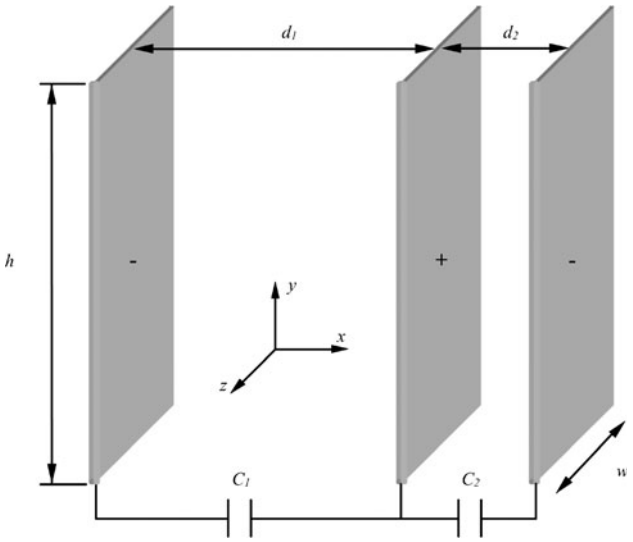

Figure 5. Interdigitated offset comb capacitors.

where K is the dielectric constant for the material (for air $K = 1$) and ε is the permittivity of free space that is equal to $8.8542 \times 10^{-12}\,\mathrm{C^2\,N^{-1}\,m^{-2}}$. Let C_x denote $\partial C_{\mathrm{total}}/\partial x$ and C_y denote $\partial C_{\mathrm{total}}/\partial y$,

$$C_x/C_y = (h - |\Delta y|)\frac{(2\Delta x + d_1 - d_2)}{[-\Delta x^2 - \Delta x(d_1 - d_2) + d_1 d_2]}. \qquad (3)$$

Let $\Delta y \to 0$ and $\Delta x \to d_2$. It can be seen that $C_x/C_y \to \infty$, demonstrating that selectivity of capacitance change in x and y is achieved. This selectivity was also verified in simulations using FEA as shown in figures 6 and 7.

To model the interdigitated capacitance, $C = Q/V$ relates the charge stored on one plate to the potential of the plate relative to the reference potential. Laplace's equation describes the electrostatic behavior of the potential ϕ everywhere in a charge-free space, given a particular set of boundary conditions,

$$\frac{\partial^2\phi}{\partial x^2} + \frac{\partial^2\phi}{\partial y^2} + \frac{\partial^2\phi}{\partial z^2} = 0. \qquad (4)$$

Then the electric field is

$$\vec{E} = -\nabla\phi = -\frac{\partial\phi}{\partial x} \times \vec{i} - \frac{\partial\phi}{\partial y} \times \vec{j} - \frac{\partial\phi}{\partial z} \times \vec{k}. \qquad (5)$$

Gauss's law describes the total charge Q inside a closed surface S using the surface integral of the outward-normal electric field. If $\vec{n}$ is the outward-normal unit vector for the closed surface S, then

$$Q = K\varepsilon \oint_S \vec{E} \cdot \vec{n}\,\mathrm{d}A. \qquad (6)$$

If S is chosen to be the surface of a conducting plate, then $K\varepsilon\vec{E}\cdot\vec{n}$ is the charge density at each point on the plate surface, and Gauss's law represents the surface integral of the charge density.

This set of equations was solved numerically. Figure 6 shows the electric field distribution of three adjacent offset comb capacitor plates. The key to interpreting the distribution is that the charge density on the surface of a plate is inversely proportional to the spacing of the equipotential curves adjacent to the plate surface. The greater the spacing, the lower the charge density. Thus, the capacitance between plate 2 and plate 3 is much lower than that between plate 1 and plate 2. In the simulations, the fringing fields were taken into account.

Figure 7 shows the combined structural and electrostatic analysis results using FEA where the fringing field effects are included. A 0.1 μN force causes a capacitance change of 0.05 pF.

3. Fabrication

3.1. Fabrication sequence

Fabrication was conducted in the Microtechnology Laboratory at the University of Minnesota. The main processing steps are illustrated in figure 8.

Step A. Start from a double polished p-type wafer with crystal orientation of ⟨100⟩.
Step B. LPCVD (low pressure chemical vapor deposition) 1 μm SiO_2.
Step C. Fusion bond the wafer with SiO_2 with another p-type wafer.
Step D. CMP (chemical mechanical polishing) the top wafer down to 50 μm; this forms an SOI (silicon-on-insulator) wafer. The above four steps can be replaced by directly purchasing SOI wafers.
Step E. E-beam evaporate Al to form ohmic contacts, liftoff to pattern Al.
Step F. DRIE (deep reactive ion etching) to form the features on the back side such as the outer frame and movable plates. The buried 1 μm SiO_2 layer acts as an etch stop layer and also as an insulator between the capacitors.
Step G. DRIE the top side to form capacitive comb fingers and curved springs. The devices were connected to the device wafer only by the buried SiO_2 layer.
Step H. RIE (reactive ion etching) to remove the buried SiO_2 layer. The released devices placed themselves on a carrier dummy wafer below the device wafer, and then were picked up individually from the carrier dummy wafer. The dice-free release process protects fragile structures from being damaged.

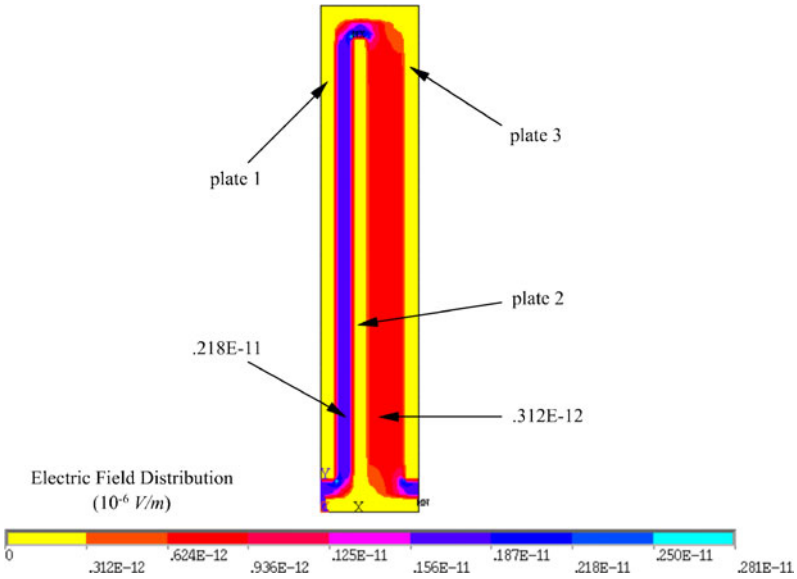

Figure 6. Electric field distribution.

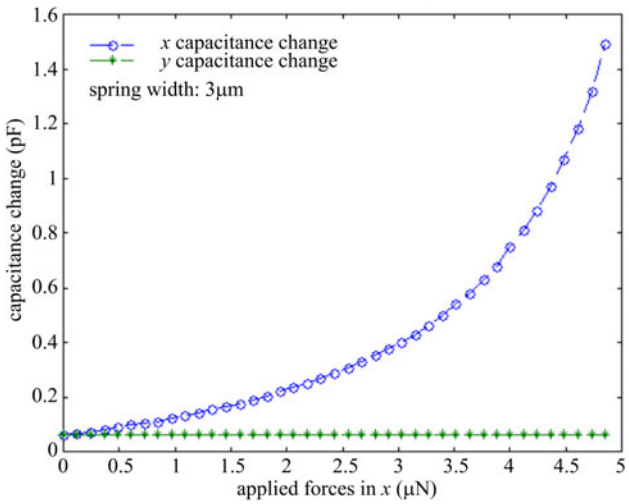

Figure 7. Capacitance change when forces are applied in *x*.

Wire bonding and packaging were undertaken respectively in the Microtechnology Laboratory and the Advanced Microsystems Laboratory. Figure 9 shows the completed device.

3.2. DRIE on SOI wafers

The deep trench etcher used in the fabrication process is a PlasmaTherm SLR-770 inductively coupled plasma reactive ion etcher using the standard Bosch process. Passivation is achieved by C_4F_8, and silicon etch by SF_6. In the beginning stage of processing, serious notching or footing effects arose due to the differential charging of sidewalls and bottoms of features [20–24]. Between the interface of Si and SiO_2, notching can laterally extend several microns. Another serious issue in DRIE on SOI experienced in the processing was the bowing effect [23] which makes etching near the mask opening isotropic. Figure 10(*a*) shows that comb fingers of Si below the SiO_2 etch mask are undesirably removed because of the notching and bowing effects, causing the SiO_2 etch mask to float. The effects are more severe on small openings than on larger ones. Large openings have more free space for the ions to pass through without striking the sidewalls and are less sensitive to these effects. The notching effect has been theoretically investigated using the sheath model [20, 22, 24]. It has been proposed that to minimize these effects, one should design a mask having a uniform pattern width and large anchors that are tolerant of the notching and bowing. However, it is not always feasible to make the pattern sufficiently uniform in one design.

Recently, a DRIE tool from Surface Technology Systems integrates an additional low frequency RF power source connected to a single-turn coil around the processing chamber. This essentially allows ions to escape more readily from deep trenches after the etching cycle, minimizing notching and bowing effects. Even though this is encouraging for high aspect ratio etching in DRIE on SOI, it is not available for other existing DRIE equipment, such as the PlasmaTherm SLR-770.

In the investigation, three methods were used to significantly overcome notching and bowing effects. First, photoresist etch masks were used instead of SiO_2. It is well known that the selectivity of SiO_2 etch masks is high in DRIE. When SiO_2 etch mask is used, the localized chemistry of the plasma can be effected. The oxygen released by etching SiO_2 partially consumes the carbon from the C_4F_8 used for passivation, while a photoresist etch mask brings extra carbon into the local environment. Experimentation demonstrated that using photoresist etch masks significantly reduces notching and bowing effects than SiO_2 with the same flow rate of C_4F_8. Second, passivation effects were enhanced in the processing by lengthening the passivation time and lowering etching power. Notching and bowing effects occur and are aggravated when the sidewall passivation polymer is removed faster than it forms. To achieve satisfactory passivation effects, it is desirable to either increase the flow rate of C_4F_8 or lengthen the time period of the passivation cycle

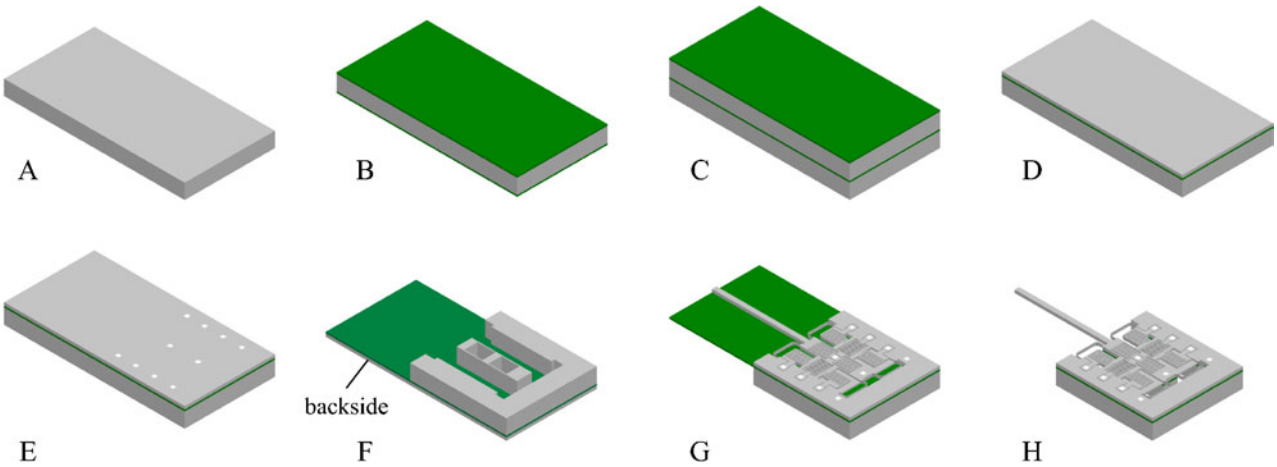

Figure 8. Fabrication sequence.

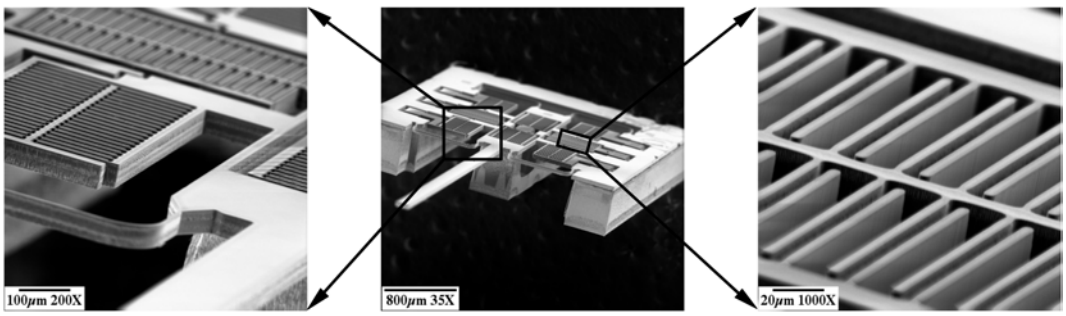

Figure 9. SEM micrograph of the device.

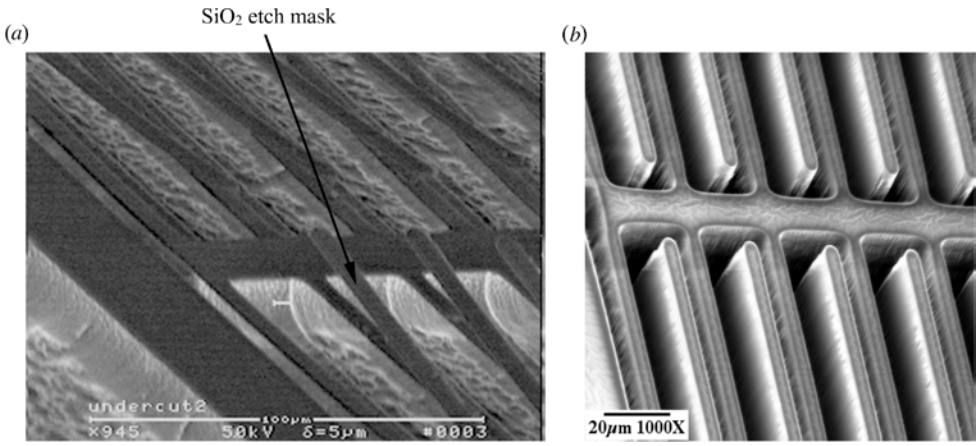

Figure 10. Overcome the notching and bowing effects.

in DRIE. In the processing, the passivation time was increased from 5 s as in the standard Bosch process to 6 s to enhance the passivation effects. The alternative method adopted to enhance the passivation effects was to lower the etching power in the etching cycle. The etching power was decreased from 9 W to 7 W. This lowered etching power decreased the etch rate as expected. However, by lengthening the passivation cycle and decreasing the etching power, the bowing and notching effects were greatly reduced due to the enhanced passivation effects. Third, enhanced heat conduction was introduced into the etch process. The Bosch process for DRIE is sensitive to temperature change. When temperature increases, passivation effects deteriorate. Conversely, when temperature decreases, the efficiency of polymer deposition is increased while the etch rate is not greatly affected. Thus, varying chamber temperature can be an alternative way of controlling etch profile. It was determined that when heat from the ICP brings the wafer temperature over 100 °C, etching becomes isotropic. A heat conductive paste from AITechnology (Cool-grease 7016) was used to bond the device wafer to a carrier wafer instead of directly applying photoresist for bonding, which facilitated cooling from helium on the chuck.

Combining the above three techniques, DRIE on SOI was successfully conducted. Features as small as 2 μm survived the notching and bowing effects during the 50 μm etching process as shown in figure 10(*b*).

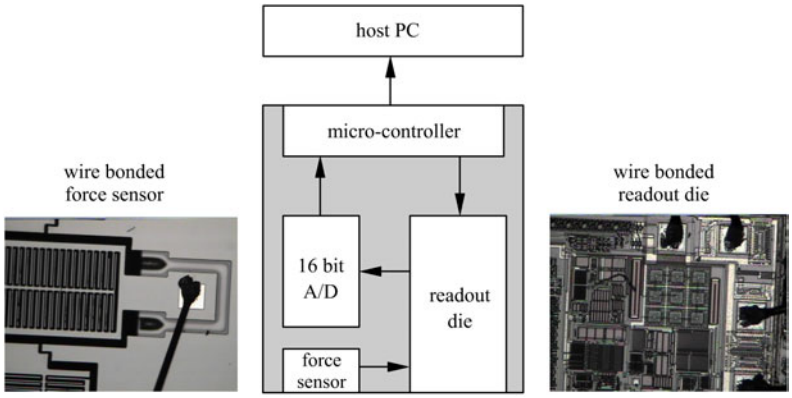

Figure 11. Readout circuit design.

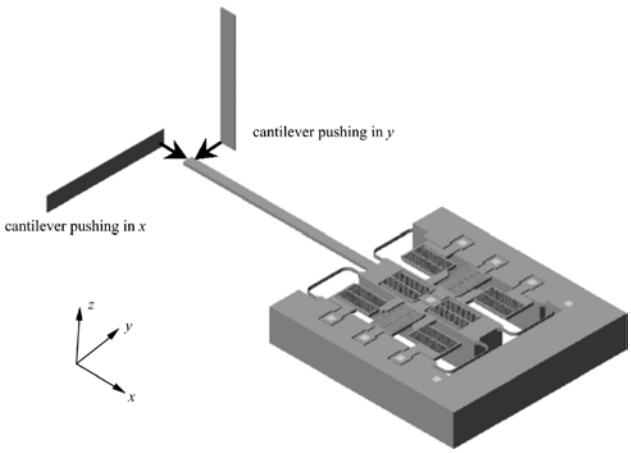

Figure 12. Calibration system setup.

4. Readout circuit design

A capacitive readout ASIC, the MS3110 from MicroSensors with a resolution of 4.0 aF $Hz^{-1/2}$, was used to convert capacitance change into voltage change. The relationship between input capacitance change and the output voltage is strictly linear.

The force sensor was wired bonded on a circuit board shown in figure 11. A micro-controller programs the capacitance readout IC MS3110 so that the internal registers can be trimmed for accurate measurements. An on-board 16-bit A/D converter converts the analog output of the MS3110 into digital signals to decrease the voltage drop and noise. The converted digital signals are received through the micro-controller by a host PC.

5. Calibration results and discussion

Calibration was conducted using calibrated piezoresistive cantilevers and an AFM. The stiffness of the cantilevers varies from 0.1 μN μm^{-1} to 1714.29 μN μm^{-1}. The cantilevers were mounted on a 3-DOF microrobot in which the *XYZ* axes each had a travel of 2.54 cm with a step resolution of 40 nm [26]. The cantilever applies a known force to the probe of the force sensor, causing gap changes and capacitance changes, as illustrated in figure 12.

Table 2. Stiffness of devices with different spring widths.

Spring width (μm)	Stiffness in x (N m^{-1})	Stiffness in y (N m^{-1})
3	1.136	24.106
5	5.248	110.753
7	14.375	301.469
10	38.46	867.862

Table 2 lists the structural calibration results of the devices with various spring widths.

Calibration results for devices with 3 μm are shown in figure 13. Devices with four different spring widths have similar electrostatic properties (i.e., the relationship between gap change and capacitance change). They differ only in mechanical properties (i.e., the relationship between applied forces and resulting gap changes).

When large forces are applied to the probe of the force sensor in the y direction, rotatory motion occurs on the central movable plate. This rotation effect on the x direction sensing was minimized by measuring the parallel capacitance change of comb drive 1 and 4 in figure 1. Because comb drive 2 and 5 are located along the centroid, the rotation of the movable plate only causes slight translation of comb drive 2 and 5 in x. Therefore, the cross coupling in x and y was resolved.

Experiments revealed that the sensitivity of the force sensors is lower than that obtained in simulations. This is mainly due to the parasitic capacitance in series with the comb capacitors, such as from poor ohmic contact. Denoting the lumped parasitic capacitance as C_p and a set of comb drive capacitance as C_d, the measured capacitance C_m, in the model shown in figure 14, is given by

$$C_m = \frac{C_p C_d}{C_p + C_d}. \tag{7}$$

The decreased sensitivity due to the parasitic capacitance is then

$$\frac{\partial C_m}{\partial C_d} = \left(1 - \frac{C_d}{C_p + C_d}\right)^2 < 1. \tag{8}$$

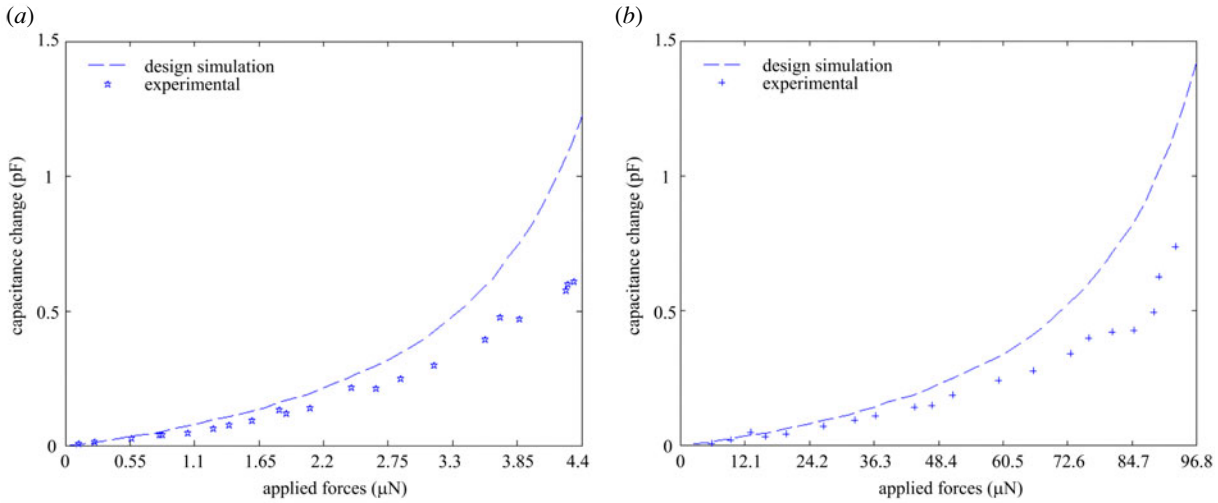

Figure 13. Calibration results for devices with 3 μm springs: (*a*) in *x* and (*b*) in *y*.

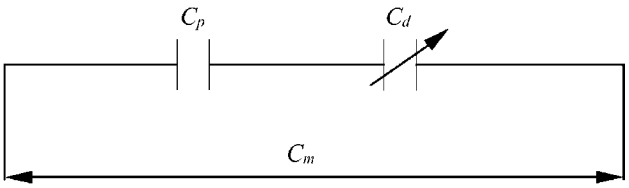

Figure 14. Parasitic capacitance in series with comb capacitors.

6. Conclusions

The complete design methodology and fabrication process of a multi-axis capacitive cellular force sensor are presented. High aspect ratio transverse comb drive structures were constructed by DRIE on SOI wafers. Notching and bowing effects for DRIE on SOI wafers were investigated. Three proposed techniques were demonstrated to be effective for overcoming the notching and bowing effects. Combining the stiffness of the force sensors, the capacitance change with applied forces and the resolution of the readout circuitry, the capability of resolving forces up to 490 μN with a resolution of 0.01 μN in *x*, and up to 900 μN with a resolution of 0.24 μN in *y* was achieved. The asymmetrical sensitivity in *x* and *y* is because the force sensing capability in *y* is to provide tangential force information generated by improperly aligned probes during microrobotic manipulation so that the orientation of the probe can be adjusted properly. System testing demonstrates that the performance was not degraded in aqueous solutions, where only the probe of the force sensors was emersed in the solutions. The intended use of the sensor is to provide real-time force feedback for microrobotic cell manipulation, such as in cell positioning, embryo pronuclei DNA injection [26] and biomembrane mechanical property modeling for cell injury and recovery studies [27].

References

[1] Charras G T, Lehenkari P P and Horton M A 2001 Atomic force microscopy can be used to mechanically stimulate osteoblasts and evaluate cellular strain distribution *Ultramicroscopy* **86** 85–95

[2] Fauver M E, Dunaway D L, Lillenfeld D H, Craighead H G and Pollack G H 1998 Microfabricated cantilevers for measurement of subcellular and molecular forces *IEEE Trans. Biomed. Eng.* **45** 891–8

[3] Guilbault G G and Luong J H 1989 Biosensors: current status and future possibilities *Ion-Sel. Electrode Rev.* **11** 3–16

[4] Lin G, Pister K S and Roos K P 1995 Novel microelectromechanical system force transducer to quantify contractile characteristics from isolated cardiac muscle cells *J. Electrochem. Soc.* **142** 31–3

[5] Lin G, Pister K S and Roos K P 2000 Surface micromachined polysilicon heart cell force transducer *J. Microelectromech. Syst.* **9** 9–17

[6] Enikov E T and Nelson B J 2000 Three-dimensional microfabrication for a multi-degree-of-freedom capacitive force sensor using fibre-chip coupling *J. Micromech. Microeng.* **4** 492–7

[7] Hirano T, Furuhata T, Gabriel K J and Fujita H 1992 Design, fabrication, and operation of submicron gap comb-drive microactuators *J. Microelectromech. Syst.* **1** 52–9

[8] Tang W C, Nguyen T H, Judy M W and Howe R T 1990 Electrostatic-comb drive of lateral polysilicon resonators *Sensors Actuators* A **21–23** 328–31

[9] Tang W C, Lim M G and Howe R T 1992 Electrostatic comb drive levitation and control method *J. Microelectromech. Syst.* **1** 170–8

[10] Yeh J L A, Jiang H and Tien N C 1999 Integrated polysilicon and DRIE bulk silicon micromachining for an electrostatic torsional actuator *J. Microelectromech. Syst.* **8** 456–65

[11] Kuehnel W and Sherman S 1994 A surface micromachined silicon accelerometer with on-chip detection circuitry *Sensors Actuators* A **45** 7–16

[12] Prasad R, MacDonald N and Taylor D 1995 Micro-instrumentation for tribological measurement *8th Int. Conf. on Solid-State Sensors and Actuators* pp 52–5

[13] Xu Y, Miller S A and MacDonald N C 1995 Microelectromechanical scanning tunneling microscope *8th Int. Conf. on Solid-State Sensors and Actuators* pp 640–3

[14] Selvakumar A and Najafi K 1998 A high-sensitivity *Z*-axis capacitive silicon microaccelerometer with a torsional suspension *J. Microelectromech. Syst.* **7** 192–200

[15] Juan W H and Pang S W 1996 Released Si microstructures fabricated by deep etching and shallow diffusion *J. Microelectromech. Syst.* **5** 18–23

[16] Lee S, Park S and Cho D 1999 The surface/bulk micromachining (SBM) process: a new method for fabricating released MEMS in single crystal silicon *J. Microelectromech. Syst.* **8** 409–16

[17] Lee S, Park S, Kim J, Lee S and Cho D 2000 Surface/bulk micromachined single-crystalline-silicon micro-gyroscope *J. Microelectromech. Syst.* **9** 557–67
[18] Takimoto S, Kondo R, Suzuki K and Sugiyama S 1999 Fabrication of micromotors using LIGA process *Int. Symp. on Micromechatronics and Human Science* pp 221–6
[19] Horsley D A, Singh A, Pisano A P and Horowitz R 1997 Angular micropositioner for disk drives *IEEE 10th Int. Workshop on Micro Electro Mechanical Systems* pp 454–9
[20] Arnold J C and Sawin H H 1991 Charging of pattern features during plasma etching *J. Appl. Phys.* **10** 5314–7
[21] Ayón A A, Ishihara K, Braff R A, Sawin H H and Schmidt M A 1999 Microfabrication and testing of suspended structures compatible with silicon-on-insulator technology *J. Vac. Sci. Technol.* B **17** 1589–93
[22] Hwang G S and Giapis K P 1997 On the origin of the notching effect during etching in uniform high density plasmas *J. Vac. Sci. Technol.* B **15** 70–87
[23] Ishihara K, Yung C F, Ayón A A and Schmidt M A 1999 An inertial sensor technology using DRIE and wafer bonding with interconnecting capability *J. Microelectromech. Syst.* **8** 403–8
[24] Kinoshita T, Hane M and McVittie J P 1996 Notching as an example of charging in uniform high density plasmas *J. Vac. Sci. Technol.* B **14** 560–5
[25] Needham D and Nunn R S 1990 Elastic deformation and failure of lipid bilayer membranes containing cholesterol *Biophys. J.* **58** 997–1009
[26] Sun Y and Nelson B J 2001 Microrobotic cell injection *IEEE Int. Conf. on Robotics and Automation* vol 1 pp 620–5
[27] Morris G J and Clarke A 1981 *Effects of Low Temperatures on Biological Membranes* New York: Academic pp 335–77